



## LETTER

## Morphology control of aligned carbon nanotube pins formed via patterned capillary densification

RECEIVED  
4 January 2019ACCEPTED FOR PUBLICATION  
14 January 2019PUBLISHED  
31 January 2019Ashley L Kaiser<sup>1</sup> , Itai Y Stein<sup>2</sup> , Kehang Cui<sup>3</sup> and Brian L Wardle<sup>2,4</sup> <sup>1</sup> Department of Materials Science and Engineering, Massachusetts Institute of Technology, Cambridge, MA 02139, United States of America<sup>2</sup> Department of Aeronautics and Astronautics, Massachusetts Institute of Technology, Cambridge, MA 02139, United States of America<sup>3</sup> Department of Mechanical Engineering, Massachusetts Institute of Technology, Cambridge, MA 02139, United States of America<sup>4</sup> Author to whom any correspondence should be addressed.E-mail: [kaisera@mit.edu](mailto:kaisera@mit.edu) and [wardle@mit.edu](mailto:wardle@mit.edu)**Keywords:** nanofibers, capillary densification, patterning, self-assembly, confinement, scaling relations, carbon nanotubesSupplementary material for this article is available [online](#)**Abstract**

The exceptional intrinsic properties of aligned nanofibers, such as carbon nanotubes (CNTs), and their ability to be easily densified by capillary forces motivates their use as shape-engineerable materials. While a variety of self-assembled CNT structures, such as cell networks, micropillars, and pins have previously been fabricated via the capillary-mediated densification of patterned CNT arrays, predicting the critical pattern size ( $s_{cr}$ ) that separates cell versus pin formation and the corresponding process-morphology scaling relations within the micrometer range are outstanding. Here, facile and scalable mechanical patterning and capillary densification techniques are used to establish  $s_{cr}$  by elucidating how the effective elastic modulus of aligned CNT arrays during densification governs the resulting pin geometries. Experiments and modeling show that this effective modulus scales with CNT height and is about an order of magnitude smaller for pins as compared to cell networks formed from bulk-scale (i.e. non-patterned) CNT arrays. Patterning therefore results in pins with a lower packing density (commensurate with double the wall thickness) and a larger characteristic length scale than bulk cell networks (i.e.  $s_{cr} \sim 5 \times$  cell width). CNT arrays with the initial randomly-oriented carbon ‘crust’ removed via oxygen plasma etching yield a higher degree of structural uniformity and better agreement with the proposed elasto-capillary model, which enables the use of capillary densification to predictively design hierarchical and shape-tunable materials for advanced thermal, electronic, and biomedical devices.

**1. Introduction**

Recent advances in the synthesis and densification of low-dimensional nanostructures, including aligned nanofibers (NFs), nanotubes, and nanoribbons, provide new opportunities for large-scale manufacturing of high-value nanomaterials [1–6]. In particular, scalable capillary-mediated densification techniques, which operate on the principles of evaporative self-assembly [7–11], are promising methods to create hierarchical and functional material structures without the need for cost-prohibitive cleanroom techniques [12, 13]. For example, solid pins and long-range cell networks can be formed by densifying aligned NF arrays within small and large pattern sizes ( $s$ ), respectively [14–17], with the critical pattern size ( $s_{cr}$ ) separating these two morphologies for a given NF height ( $h$ ) [18] (see figure 1). However, to fully realize the potential of capillary self-assembly for multiscale material design, enhanced process-structure control is necessary to predict NF densification within micron-scale  $s_{cr}$  values [18–20] by incorporating pattern-induced confinement and interfacial effects into existing models for bulk-scale densification [19–25]. In this work, we present process-morphology scaling relations to describe solid pin formation from the capillary densification of patterned aligned NF arrays of  $h < 60 \mu\text{m}$  with  $s_{cr} < 200 \mu\text{m}$ , and we demonstrate a predictive capability including the

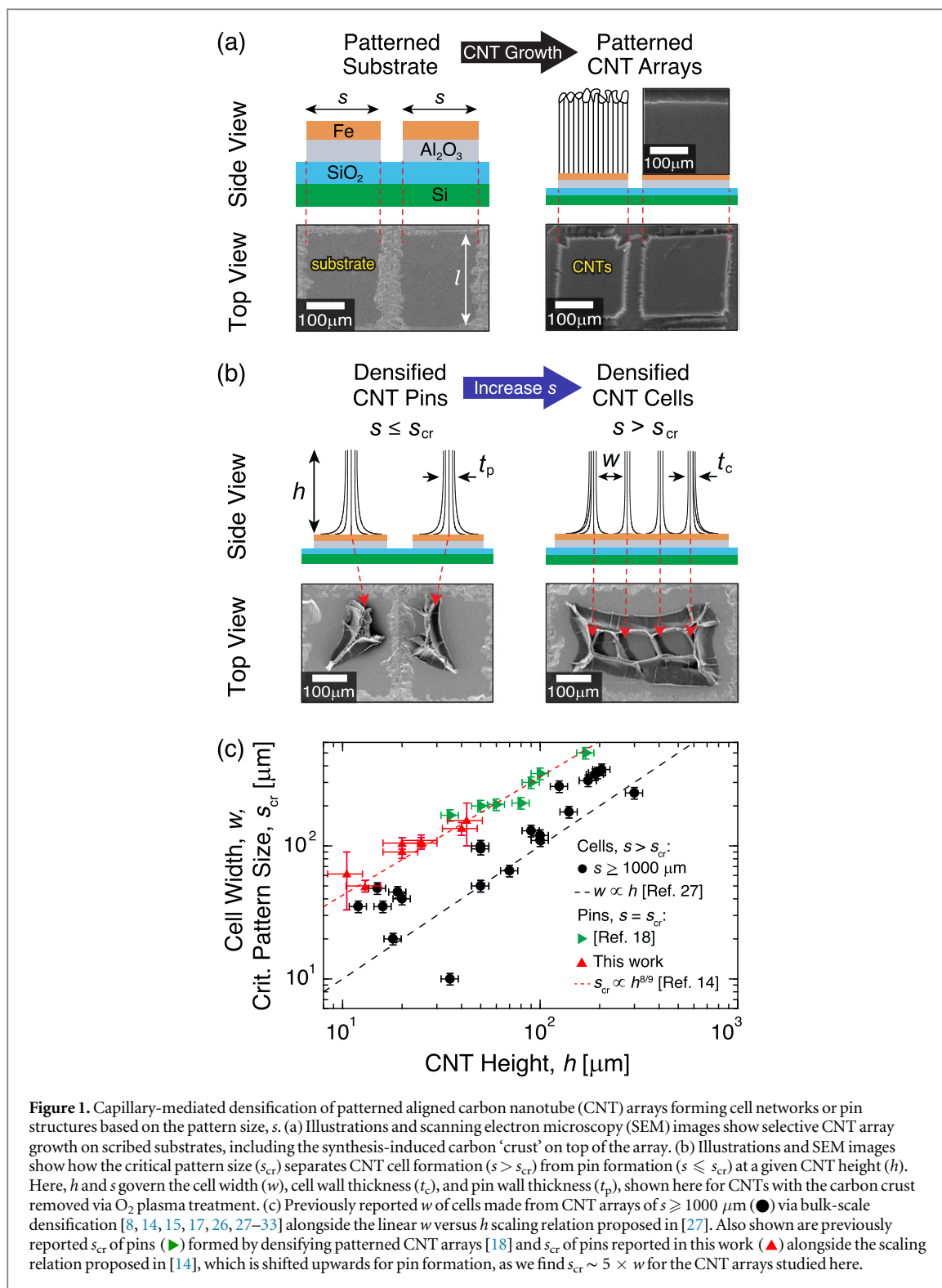


**Figure 1.** Capillary-mediated densification of patterned aligned carbon nanotube (CNT) arrays forming cell networks or pin structures based on the pattern size,  $s$ . (a) Illustrations and scanning electron microscopy (SEM) images show selective CNT array growth on scribed substrates, including the synthesis-induced carbon ‘crust’ on top of the array. (b) Illustrations and SEM images show how the critical pattern size ( $s_{\text{cr}}$ ) separates CNT cell formation ( $s > s_{\text{cr}}$ ) from pin formation ( $s \leq s_{\text{cr}}$ ) at a given CNT height ( $h$ ). Here,  $h$  and  $s$  govern the cell width ( $w$ ), cell wall thickness ( $t_c$ ), and pin wall thickness ( $t_p$ ), shown here for CNTs with the carbon crust removed via  $\text{O}_2$  plasma treatment. (c) Previously reported  $w$  of cells made from CNT arrays of  $s \geq 1000\mu\text{m}$  ( $\bullet$ ) via bulk-scale densification [8, 14, 15, 17, 26, 27–33] alongside the linear  $w$  versus  $h$  scaling relation proposed in [27]. Also shown are previously reported  $s_{\text{cr}}$  of pins ( $\blacktriangleright$ ) formed by densifying patterned CNT arrays [18] and  $s_{\text{cr}}$  of pins reported in this work ( $\blacktriangle$ ) alongside the scaling relation proposed in [14], which is shifted upwards for pin formation, as we find  $s_{\text{cr}} \sim 5 \times w$  for the CNT arrays studied here.

finding that the effective elastic modulus scaling of the pin wall with  $h$  governs the pin wall thickness, densification factor, and corresponding  $s_{\text{cr}}$  values.

Capillary densification has been used in recent years to leverage the excellent thermal, electrical, and mechanical properties of aligned carbon nanotube (CNT) arrays [34–37] by forming them into dense three-dimensional structures [8, 9, 38], which have applications as electrical interconnects [39–41], sensors and actuators [42–46], field emitters [47, 48], and z-direction composite reinforcement [49, 50]. While these geometrically complex microstructures can be formed by growing and then densifying patterned CNT arrays [8, 16] (see figure 1), it is currently challenging to control the densified CNT morphology as a function of  $h$  and  $s$ , especially without incurring the cost and process hurdles of cleanroom techniques. Spatially selective CNT array

growth has previously been achieved by patterning catalyst layers via photo- and electron-beam-lithography [51, 52] and by using metallic layers as catalyst deactivators [53–55], but these processes are time-consuming and cost-prohibitive at large scales. Additionally, they often produce fragile CNT arrays with synthesis-induced structural variations [56–58] and a low density per unit area [59, 60], which collectively yield properties that can be orders of magnitude below theoretical values [61–63]. To overcome these limitations, scalable processing techniques, such as simple catalyst patterning via mechanical scribing [26, 64, 65] (figure 1(a)), post-CNT-growth O<sub>2</sub> plasma treatment to increase structural uniformity [18], and capillary densification (figure 1(b)) are attractive methods to create high-density, morphology-controlled bulk nanostructured materials provided that models can guide the processing towards these desired structures.

Previous model development has focused on the self-assembly of fiber arrays undergoing bulk-scale (i.e. non-patterned and cell-forming) capillary densification [9, 21–25], including the well-characterized formation of cell networks from bulk-scale aligned CNT arrays [14, 26, 27–33]. While cells are desirable for long-range open structures, patterned CNT array densification offers new capabilities to create relatively dense pins needed for nano- and micron-scale device-specific geometries [66–68]. Accurately predicting densified CNT morphologies in this regime is not yet possible, particularly for dense pin geometries with  $s_{cr} < 200 \mu\text{m}$  [8, 18] (see figure 1(c)). Experimentally-validated models are needed to explain the confinement and interfacial effects governing patterned densification. Through extensive quantification of aligned CNT pins forming at  $s_{cr}$  as a function of  $h$  and O<sub>2</sub> plasma treatment, we model the mechanical behavior of CNT array densification and show that previous theories for the elasto-capillary self-assembly of bulk-scale CNTs [9, 14] can also be applied to the densification of patterned CNTs, when appropriate (but counter to prior work) pin wall moduli and volume fractions are incorporated. We show that the effective elastic modulus scaling of the pin wall with  $h$  governs CNT pin formation and is about an order of magnitude smaller compared to bulk-scale cell formation, a direct result of dominating interfacial effects in patterned CNT densification to pins.

## 2. Methods

We synthesized and densified patterned aligned CNT arrays to study samples of varying heights and plasma treatments. Capillary-densified CNT geometries were measured via scanning electron microscopy (SEM), and an elasto-capillary model was used to develop the scaling relations for CNT pin morphology *at the critical* pattern size ( $s_{cr}$ , i.e. pin not cell formation) as a function of CNT height.

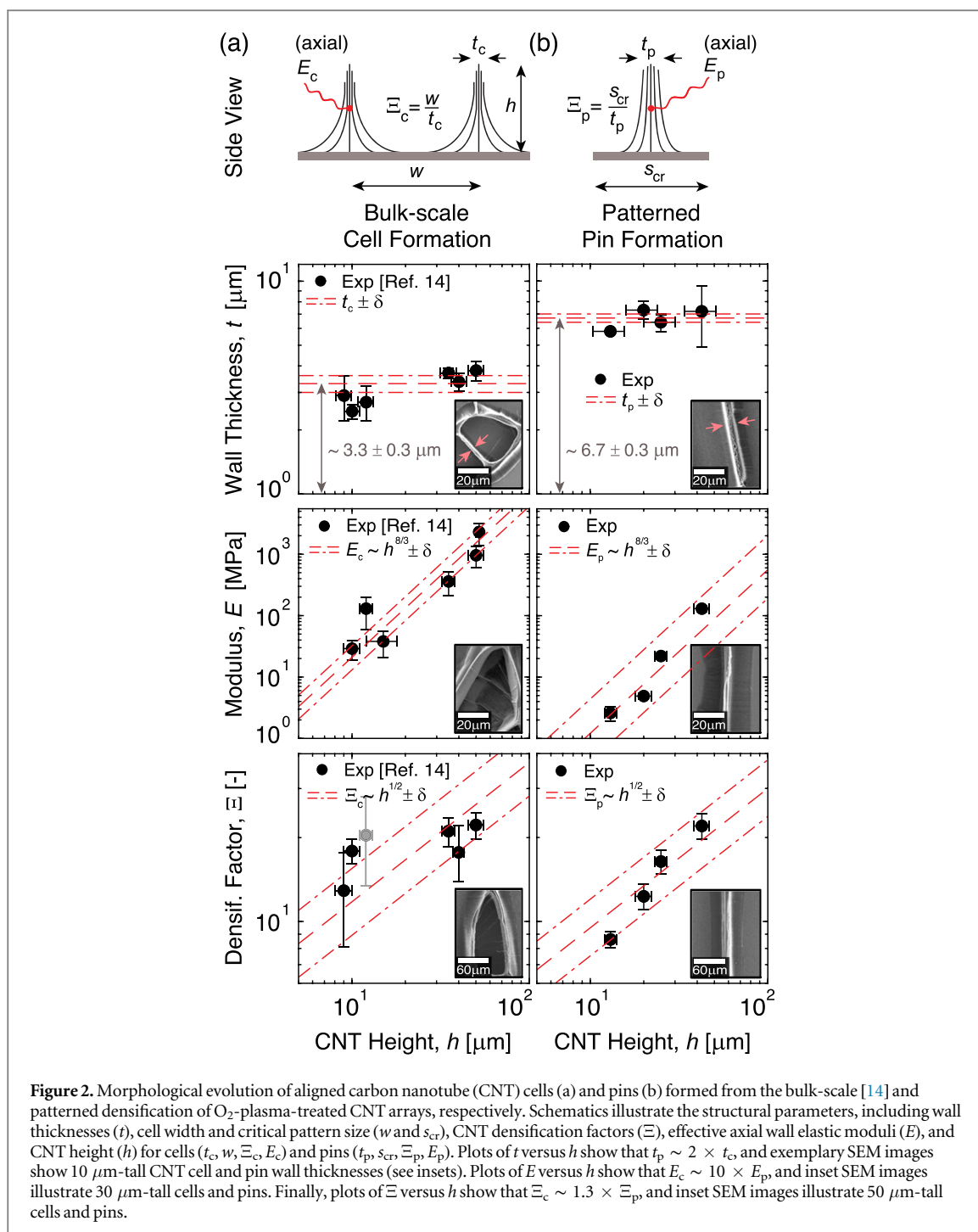
### 2.1. Substrate patterning and CNT synthesis

To create patterned CNT arrays as pin precursors, SiO<sub>2</sub>/Si wafers were first coated with a 10 nm Al<sub>2</sub>O<sub>3</sub> and a 1 nm Fe layer deposited via electron beam physical vapor deposition [69, 70]. These substrates were cut into 1 cm × 1 cm squares and mechanically scribed by hand to remove the Fe/Al<sub>2</sub>O<sub>3</sub> catalyst layers in outlined grid patterns of rectangular dimensions  $s \times l$ , as shown in figure 1(a). Due to the selective removal of catalyst in the ~40 μm wide grid lines, CNT arrays only grow inside the rectangular pattern where the catalyst remains. Here,  $l \gg s$  so that the densified CNT pin wall thickness ( $t_p$ ) at the critical pattern size ( $s_{cr}$ ) can be measured laterally across the center of the pin, representing one-dimensional densification of the CNT array away from the pattern edges (see figure 2 and section S1 of the supplementary material available online at [stacks.iop.org/NANOF/3/011003/mmedia](https://stacks.iop.org/NANOF/3/011003/mmedia)). Corner effects resulting from biaxial densification at the pin ends are not considered here, as they would dominate the formation of complex pillar shapes when  $l$  approaches  $s$ , as shown by SEM images in figure 1(b).

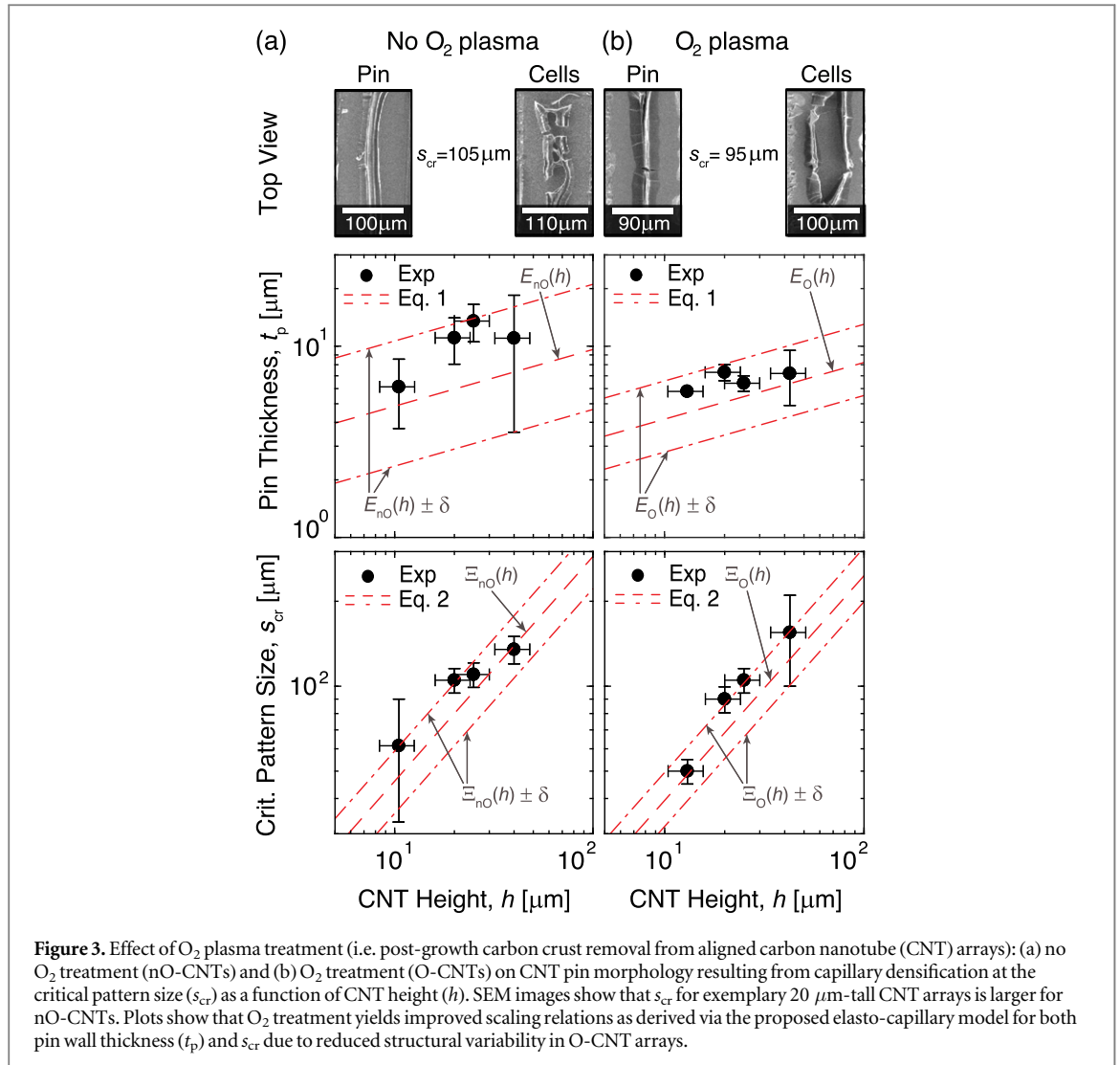
Following substrate patterning, vertically-aligned CNT arrays were grown by a base-growth mechanism in a 22 mm internal diameter quartz tube furnace at atmospheric pressure via a previously-described thermal catalytic chemical vapor deposition process, which uses ethylene as the carbon source and 600 ppm of water vapor added to the inert gas, allowing cm-scale CNT arrays to be grown [71–73]. In each pattern, the growing CNTs self-assemble into aligned arrays of height ( $h$ ) ~ 10–50 μm, controlled by growth time and measured via optical microscopy. The arrays are comprised of multiwalled CNTs with an average outer diameter of ~8 nm (3–7 walls with ~5–6 nm inner diameter and intrinsic CNT density of  $\approx 1.6 \text{ g cm}^{-3}$ ) [73–75], inter-CNT spacing of ~60–80 nm [76, 77], and volume fraction of ~1% CNTs [73].

### 2.2. Capillary densification

After growth, a subset of the patterned CNT array samples were exposed to a previously-developed recipe for O<sub>2</sub> plasma treatment to remove the tangled CNT crust layer [18], which forms on top of the CNT array as a result of the growth process [56, 57] (see figure 1(a)). This leads to non-O<sub>2</sub>-treated CNTs (nO-CNTs) and O<sub>2</sub>-treated CNTs (O-CNTs) to investigate the effect of the carbon crust constraint on densification as a secondary objective. All CNT arrays were then densified via a previously reported paper-soaking technique



[78] using acetone, as this process enables more controlled wetting (via the hydrodynamics of acetone leaving the paper) to avoid CNT delamination from the substrate, compared to direct immersion procedures [8]. After capillary densification,  $s_{cr}$  values of the CNT pins were measured via SEM (Zeiss Merlin, 5 mm working distance, 5 kV accelerating voltage) and were defined as the pattern size yielding solid pins at the transition between pin and cell formation, where any larger  $s$  would initiate cell formation inside the pin structure (see figure 1(b)). Since a variety of pattern sizes were scribed in the substrate, many pins at  $s_{cr}$ , cell networks above  $s_{cr}$ , and pins below  $s_{cr}$  could be located on one sample, and only the pins at  $s_{cr}$  were considered in this work. Then, pin wall thickness ( $t_p$ ) at  $s_{cr}$  as a function of  $h$  was measured via SEM, and the  $h$  dependence of  $t_p$  and  $s_{cr}$  was investigated by averaging these values from 3–4 samples. This is presented in figure 2 for comparison between bulk-scale CNT cell networks and O-CNT pins, figure 3 for comparison between nO- and O-CNT pins, and table S1 in section S3 of the supplementary material.



### 2.3. Modeling of capillary-densified CNT pins

The capillary-mediated self-organization of patterned CNT arrays into pin structures at  $s_{cr}$  is modeled via a one-dimensional mechanism following previous work describing the densification of bulk-scale CNT arrays into cell networks, which used the same paper-soaking densification procedure [14]. Here,  $t_p$  is estimated from the maximum elasto-capillary bundle size [9, 25, 79] by considering the patterned CNT array morphology [58, 75, 76], yielding the following relation:

$$t_p \approx \Gamma_f \left( \left( \frac{\gamma}{E_p} \right)^{2/3} \left( \frac{4h^{8/3}}{D_{cnt}^2 \Gamma_i^{4/3}} \right) \right)^{1/3}, \quad (1)$$

where  $\gamma$  is the surface tension of the solvent ( $25 \times 10^{-3} \text{ N m}^{-1}$  for acetone),  $E_p$  is the effective axial elastic modulus of the pin wall (calculated via equation (1)) that corresponds to the collective elastic response of the wavy CNT array,  $\Gamma_i$  and  $\Gamma_f$  are the initial (i.e. as-grown) and final (i.e. densified) inter-CNT spacings,  $D_{cnt}$  is the CNT outer diameter, and  $h$  is the measured CNT height. As discussed in section S1 of the supplementary material, a one-dimensional unit cell of size  $s_{cr}$  is defined so that  $s_{cr}$  can be estimated from  $t_p$  as follows, assuming thorough solvent wetting [80] and that all CNTs within  $s_{cr}$  comprise the pin wall after densification:

$$s_{cr} \approx t_p \Xi_p, \quad (2)$$

where  $\Xi_p$  is the one-dimensional densification factor.  $\Xi_p$  describes the increase in CNT array packing density as a result of the elasto-capillary self-assembly process and is discussed further in section S1 of the supplementary material, along with the estimations of  $\Gamma_i$  and  $\Gamma_f$ . Using equations (1) and (2), the experimentally-quantified  $t_p$  values and calculated  $E_p$  and  $\Xi_p$  values in figures 2 and 3 for O-CNTs (i.e.  $E_O$  and  $\Xi_O$ ) can be analyzed. This framework is also applied to analyze the  $t_p$ ,  $s_{cr}$ ,  $E_{nO}$ , and  $\Xi_{nO}$  scaling of pins presented in figure 3 as a comparison between nO- and O-CNTs.

### 3. Results and discussion

We compared the morphological evolution of capillary-densified cell networks that formed from bulk-scale O-CNT arrays with pins that formed at  $s_{cr}$  from patterned O-CNT arrays, including the wall thicknesses, effective elastic wall moduli, and densification factors (i.e. CNT packing density within the cell and pin walls). We then used the elasto-capillary model to compare these parameters, including the scaling of  $t_p$  and  $s_{cr}$  with  $h$ , for pins that formed from patterned nO- and O-CNT arrays.

#### 3.1. Comparison of O<sub>2</sub>-treated CNT cells and pins

As figure 2 illustrates, similar schematics describe the geometries of cell [14] and pin structures resulting from the capillary densification of aligned CNT arrays. These structures are differentiated by the one-dimensional length across which densification occurs, as bulk-scale cells exhibit a characteristic length approximately equal to the cell width ( $w$ ), while pins forming at their critical pattern size are confined to densify within the scribed length of  $s_{cr}$ . While the cell and pin wall thicknesses ( $t_c$  and  $t_p$ ) scale almost linearly with  $h$  (as shown in figure 3 and in previous work [14]), average  $t$  values can be used to compare the relative magnitude of  $t_c$  and  $t_p$ . Here, figure 2 shows that  $t_p \sim 2 \times t_c$  as  $s$  approaches  $s_{cr}$ , which can be understood as an imaginary ‘cell’ inside of the CNT array collapsing during densification to form the solid pin structure.

For both cell and pin morphologies, previous work showed that a higher degree of densification at a given  $h$  is linked to a higher wall modulus and lower wall thickness, as a correspondingly thinner, stiffer, and denser wall can better support the load from capillary forces [8, 14, 81]. However, the overall magnitude and scaling of these parameters with  $h$  and  $s$  will depend upon the ability of CNTs to self-organize in the most energetically preferential manner, which would result in the highest packing densities [8, 76, 82], but such ideal packing may not be allowed if the CNTs are forced to densify along a specific direction due to their confinement within a pattern. To investigate this scenario, which applies to the pins formed here, one can describe a patterned CNT array as having a more ‘unconstrained’ perimeter (i.e. fewer CNT–CNT sidewall interactions) compared to the same CNTs within a bulk-scale array, where the surrounding CNTs increase the extent of such interactions. Relative to its size, a patterned array also has enlarged solvent-air interfaces along its perimeter during solvent evaporation, which influences the spatial trajectory of densifying CNTs owing to the greater difference in hydrostatic dilation stress created across these interfaces [29, 81]. Therefore, as previous studies on patterned CNT densification have shown [26, 29, 81], CNT translation is directed laterally towards the center of the pattern due to the solvent-air interfaces receding from the array and a thin solvent layer remaining pinned to the outer CNTs via surface tension, which act to push the CNT array inwards. This process is also aided by fewer CNT–CNT sidewall interactions present along the perimeter that could force CNT translation in other directions (which occurs in bulk-scale cell network formation). These interfacial effects are consistent with prior observations of wetted CNT arrays densifying from low-density to high-density regions under capillary forces [26, 29, 81].

The consequences of such effects can be observed in the patterned CNT arrays used here by comparing the different morphological evolution of O-CNT cells and pins. These differences are revealed by the scaling of  $E$  and  $\Xi$  with  $h$  (figure 2), which shows that  $E_p$  and  $\Xi_p$  evolve similarly but are generally smaller than  $E_c$  and  $\Xi_c$  [14]. Here,  $E_c$  and  $E_p$  both scale as  $h^{8/3}$ , which can be estimated as  $E \propto \alpha(h)^\psi$ , where  $\alpha_c \approx 0.030 \pm 0.006 \propto 10 \times \alpha_p$  and  $\psi_c = \psi_p \approx 8/3$ . Because they are longer, taller CNTs inherently have more connections between them to reinforce the array, and hence  $E$  has been observed to scale with  $h$  [14, 61]. Similarly,  $\Xi_c$  and  $\Xi_p$  both scale as  $h^{0.5}$ , which is estimated here as  $\Xi \propto \beta(h)^\omega$ , where  $\beta_c \approx 3.7 \pm 1 \propto 1.3 \times \beta_p$  and  $\omega_c = \omega_p \approx 0.5$ . This scaling leads to  $t_c < t_p$  at a given  $h$  and is consistent with patterned densification reducing the effective pin wall stiffness and volume fraction. Therefore, the effective axial array modulus of the pin wall, and not the orders-of-magnitude higher isolated CNT axial modulus [83] governs the one-dimensional densification of patterned CNT arrays, similar to bulk-scale arrays.

Finally, since these CNTs are forced to densify towards the center of their pattern and thus do not pack as tightly as bulk-scale arrays, larger densification lengths (i.e.  $s_{cr} > w$ ) and lower CNT wall volume fractions and stiffnesses are observed for pins versus cells, especially for small  $h$  (i.e. lower overall surface areas), where the elasto-capillary pairing efficacy of neighboring CNTs is reduced [8, 9, 18]. The directive interfacial factors increasing this characteristic length are consistent with prior observations of increased CNT-substrate adhesion hindering CNT mobility, as this also resulted in larger cell widths with thicker cell walls and a lower stiffness [14]. Taken together, these interfacial effects could provide versatile methods to direct the densification process in the future and control the resulting CNT geometries.

#### 3.2. Comparison of O<sub>2</sub>-treated and non-treated pins

Next, to establish scaling relations for  $s_{cr}$  and  $t_p$  as a function of  $h$  via the elasto-capillary model, and to investigate the effect of the synthesis-induced carbon crust [12, 18, 56] (figure 1(a)) on CNT array densification, pin

geometries resulting from the densification of patterned nO- and O-CNT arrays are compared. Figure 3 illustrates that  $s_{cr}$  is larger on average for nO-CNTs, as the crust is presumed to partially restrict elasto-capillary pairing and overall CNT mobility by preventing nO-CNTs from properly reinforcing one another via free translation across the substrate [18]. Therefore, since nO-CNT densification is slightly hindered compared to O-CNTs, nO-CNTs often need to form thicker pin walls to support the capillary forces and exhibit more variable  $E_{nO}$  and  $\Xi_{nO}$  scaling with  $h$ , as discussed further in section S2 of the supplementary material. This mechanism is consistent with previous results for the densification of bulk-scale CNT arrays with increased substrate adhesion (achieved via thermal post-processing), as those resulting cells also exhibited a larger average wall thickness, cell width, and smaller effective wall stiffness due to reduced CNT mobility [14].

As figure 3 shows, the scaling of  $t_p$  and  $s_{cr}$  with  $h$  (equations (1) and (2), respectively) for both nO- and O-CNTs can be accurately represented by the governing elasto-capillary mechanics via the one-dimensional model. Owing to the structural irregularities caused by the crust, less variable scaling with  $h$  is seen for O-CNT pins, which is similar to previous work showing enhanced densification and lower structural variation within densified O-CNT micropillars [8, 18]. Removing the crust constraint allows for easier and more energetically preferential densification due to enhanced CNT mobility, yielding better agreement with the proposed densification model [9, 25, 79] as a means to enable the tunable fabrication of highly precise and uniform CNT microstructures.

The results presented here for CNT arrays of  $h < 60 \mu\text{m}$  with  $s_{cr} < 200 \mu\text{m}$  also provide insight into the discrepancies between past experimental results and analytical models for capillary densification, which can significantly overestimate the  $h$  values required to form densified cell and pin structures within pattern sizes below  $150 \mu\text{m}$  [18–20]. These models commonly set  $E$  equal to the individual CNT axial elastic modulus of 1 TPa [83], but the effective elastic modulus of densifying CNT bundles is often orders of magnitude lower ( $\sim 1\text{MPa} - 1\text{GPa}$ ) [14, 61, 84] due to the stochastic nature of CNT packing and inherent waviness [61–63, 84]. For a given  $s_{cr}$ , these models can therefore over-predict the effective stiffness required for CNT arrays to form a pin at a given  $h$ , and experimental results (including those presented here) often show that CNT arrays exhibit a lower effective stiffness to densify at a lower  $h$  to form pin structures [14, 81]. Therefore, while the 1 TPa intrinsic CNT elastic axial modulus may be appropriate for large  $s$  and  $h$ , when the elasto-capillary pairing efficacy of CNTs is relatively strong and can overcome structural variability within the array [8, 9, 18], this assumption becomes less accurate as  $s$  and  $h$  are reduced to the micro- and nano-meter regime, where more appropriate scaling and smaller  $E$  values are required to describe capillary densification.

## 4. Conclusion

In summary, the effects of aligned CNT height and  $\text{O}_2$  plasma treatment on the capillary densification of patterned CNT arrays into pins was quantified and modeled based on the underlying elasto-capillary physics. By developing process-morphology scaling relations for pin evolution with CNT array height ( $h$ ), this work reports experimentally-validated models that enable accurate morphology control of densified pin geometries created at the critical pattern size ( $s_{cr}$ ) separating cell versus pin formation, which are applicable above and below  $s_{cr}$  with appropriate wall modulus scaling. Experimental and modeling results indicate that the pin wall effective axial elastic modulus ( $E_p$ ) and densification factor ( $\Xi_p$ ) scale with  $h$  and are smaller compared to corresponding values for cell networks formed via bulk-scale densification. This is primarily attributed to pattern-induced solvent-air interfacial effects and mechanistic CNT–CNT sidewall interactions, which also yield a larger  $s_{cr}$  and pin wall thickness compared to the cell width and cell wall thickness. Finally, applying a post-growth  $\text{O}_2$  plasma treatment yields improved agreement with scaling relations that could enable precise NF patterning in the future for applications requiring microstructural control.

Additionally, it should be noted that CNT pins formed within isotropic patterns, as opposed to the non-isotropic patterns used here, are likely to experience two-dimensional (2D) effects during densification. Modeling 2D patterned densification would require quantification of topological inhomogeneities and simulation of physical CNT–CNT interactions, including the inherent waviness in aligned CNT arrays [58, 61, 76]. Moreover, since an increased CNT-substrate adhesion force ( $F_a$ ) [85] has recently been shown to reduce CNT mobility and enable the capillary densification of taller, bulk-scale CNT arrays into wider cells with thicker walls [14], it is postulated that CNT pin geometries will scale similarly with  $F_a$ . This could provide additional tunability over densified CNT architectures by using  $F_a$  as a design parameter, potentially enabling the densification of aligned CNT arrays into mm- to cm-scale structures at large  $F_a$ . Further work is required in this area, since characterization and modeling of the physiochemical mechanisms governing  $F_a$  scaling with processing and the corresponding  $F_a$  effects on CNT elasto-capillary mechanics are not currently available. Once experimentally-validated models are developed to accurately predict 2D densification and  $F_a$  effects, capillary densification may be used as a versatile method to create materials with controlled shapes, densities, and

functionalities for next-generation composite reinforcement, flexible electronics, optoelectronics, and other emerging nanoscale applications.

## Acknowledgments

This work was partially supported by Airbus, ANSYS, Embraer, Lockheed Martin, Saab AB, Saertex, and Teijin Carbon America through MIT's Nano-Engineered Composite aerospace Structures (NECST) Consortium, and partially supported by the National Aeronautics and Space Administration (NASA) Space Technology Research Institute (STRI) for Ultra-Strong Composites by Computational Design (US-COMP), grant number NNX17AJ32G. ALK was supported by the Department of Defense (DoD) through the National Defense Science and Engineering Graduate Fellowship (NDSEG) Program. At MIT, the authors thank Dr S Kim and Professor A J Hart for help with O<sub>2</sub> plasma treatment, the members of necslab for technical support and advice, and Professor C V Thompson and Professor M J Cima for helpful discussions. This work made use of the MIT Materials Research Laboratory (MRL) Shared Experimental Facilities, supported in part by the MRSEC Program of the National Science Foundation under award number DMR-1419807, and was carried out in part through the use of MIT's Microsystems Technology Laboratories.

## ORCID iDs

Ashley L Kaiser  <https://orcid.org/0000-0002-6304-6992>

Itai Y Stein  <https://orcid.org/0000-0003-3229-7315>

Kehang Cui  <https://orcid.org/0000-0002-1768-0845>

Brian L Wardle  <https://orcid.org/0000-0003-3530-5819>

## References

- [1] Zhang Y, Zhang F, Yan Z, Ma Q, Li X, Huang Y and Rogers J A 2017 *Nat. Rev. Mater.* **2** 17019
- [2] Kenry K and Lim C T 2017 *Prog. Polym. Sci.* **70** 1–17
- [3] Zhang R, Zhang Y and Wei F 2017 *Chem. Soc. Rev.* **46** 3661–715
- [4] Chen L F, Feng Y, Liang H W, Wu Z Y and Yu S H 2017 *Adv. Energy Mater.* **7** 1700826
- [5] Bai Y *et al* 2018 *Nat. Nanotechnol.* **13** 589–95
- [6] McLean B, Eveleens C A, Mitchell I, Webber G B and Page A J 2017 *Phys. Chem. Chem. Phys.* **19** 26466–94
- [7] Bico J, Reyssat E and Roman B 2018 *Annu. Rev. Fluid Mech.* **50** 629–59
- [8] De Volder M and Hart A J 2013 *Angew. Chem. Int. Ed.* **52** 2412–25
- [9] Tawfick S H, Bico J and Barcelo S 2016 *MRS Bull.* **41** 108–14
- [10] Tan A T L, Beroz J, Kolle M and Hart A J 2018 *Adv. Mater.* **30** 1803620
- [11] Pokroy B, Kang S H, Mahadevan L and Aizenberg J 2009 *Science* **323** 237–40
- [12] De Volder M, Tawfick S H, Park S J, Copic D, Zhao Z, Lu W and Hart A J 2010 *Adv. Mater.* **22** 4384–9
- [13] Tawfick S, Zhao Z, Maschmann M, Brieland-Shoultz A, De Volder M, Baur J W, Lu W and Hart A J 2013 *Langmuir* **29** 5190–8
- [14] Kaiser A L, Stein I Y, Cui K and Wardle B L 2018 *Phys. Chem. Chem. Phys.* **20** 3876–81
- [15] Zhang K, Li T, Ling L, Lu H, Tang L, Li C, Wang L and Yao Y 2017 *Carbon* **114** 435–40
- [16] De Volder M F L, Tawfick S, Park S J and Hart A J 2011 *ACS Nano* **5** 7310–7
- [17] Qiu A and Bahr D F 2013 *Carbon* **55** 335–42
- [18] De Volder M, Park S J, Tawfick S H, Vidaud D O and Hart A J 2011 *J. Micromech. Microeng.* **21** 045033
- [19] Journet C, Moulinet S, Ybert C, Purcell S T and Bocquet L 2005 *Europhys. Lett.* **71** 104
- [20] Zhao Y P and Fan J G 2006 *Appl. Phys. Lett.* **88** 103123
- [21] Sengab A and Picu R C 2018 *Phys. Rev. E* **97** 032506
- [22] Picu R C and Sengab A 2018 *Soft Matter* **14** 2254–66
- [23] Zhou M, Tian Y, Zeng H, Pesika N and Israelachvili J 2015 *Adv. Mater. Interfaces* **2** 1400466
- [24] Zhou M, Chen K, Li X, Liu L, Mo Y, Jin L, Li L and Tian Y 2018 *Langmuir* **34** 11629–36
- [25] Chiodi F, Roman B and Bico J 2010 *Europhys. Lett.* **90** 44006
- [26] Liu H, Li S, Zhai J, Li H, Zheng Q, Jiang L and Zhu D 2004 *Angew. Chem. Int. Ed.* **43** 1146–9
- [27] Chakrapani N, Wei B, Carrillo A, Ajayan P M and Kane R S 2004 *Proc. Natl Acad. Sci. USA* **101** 4009–12
- [28] Kaur S, Sahoo S, Ajayan P and Kane R 2007 *Adv. Mater.* **19** 2984–7
- [29] Li Q, DePaula R, Zhang X, Zheng L, Arendt P N, Mueller F M, Zhu Y T and Tu Y 2006 *Nanotechnology* **17** 4533
- [30] Correa-Duarte M A, Wagner N, Rojas-Chapana J, Morszeck C, Thie M and Giersig M 2004 *Nano Lett.* **4** 2233–6
- [31] Dumeé L F, Sears K, Schutz J A, Finn N, Duke M, Mudie S, Kirby N and Gray S 2013 *J. Colloid Interface Sci.* **407** 556–60
- [32] Qu J, Zhao Z, Wang X and Qiu J 2011 *J. Mater. Chem.* **21** 5967–71
- [33] Futaba D N, Hata K, Yamada T, Hiraoka T, Hayamizu Y, Kakudate Y, Tanaie O, Hatori H, Yumura M and Iijima S 2006 *Nat. Mater.* **5** 987–94
- [34] De Volder M F L, Tawfick S H, Baughman R H and Hart A J 2013 *Science* **339** 535–9
- [35] Di J, Wang X, Xing Y, Zhang Y, Zhang X, Lu W, Li Q and Zhu Y T 2014 *Small* **10** 4606–25
- [36] Zhang L, Zhang G, Liu C and Fan S 2012 *Nano Lett.* **12** 4848–52
- [37] Wang F, Drzal L T, Qin Y and Huang Z 2015 *J. Mater. Sci.* **50** 1082–93
- [38] Liu Q, Li M, Gu Y, Zhang Y, Wang S, Li Q and Zhang Z 2014 *Nanoscale* **6** 4338–44
- [39] Xiang D, Wang X, Jia C, Lee T and Guo X 2016 *Chem. Rev.* **116** 4318–440

- [40] Cui K, Chiba T, Omiya S, Thurakitseree T, Zhao P, Fujii S, Kataura H, Einarsson E, Chiashi S and Maruyama S 2013 *J. Phys. Chem. Lett.* **4** 2571–6
- [41] Wu W 2017 *Nanoscale* **9** 7342–72
- [42] Zhang J, Liu X, Neri G and Pinna N 2016 *Adv. Mater.* **28** 795–831
- [43] Fennell J F, Liu S F, Azzarelli J M, Weis J G, Rochat S, Mirica K A, Ravnsbaek J B and Swager T M 2016 *Angew. Chem. Int. Ed.* **55** 1266–81
- [44] Stoychev G V and Ionov L 2016 *ACS Appl. Mater. Interfaces* **8** 24281–94
- [45] Kong L and Chen W 2014 *Adv. Mater.* **26** 1025–43
- [46] Liang Y, Sias D, Chen P J and Tawfick S 2017 *Adv. Eng. Mater.* **19** 1600845
- [47] Shin D H, Yun K N, Jeon S G, Kim J I, Saito Y, Milne W I and Lee C J 2015 *Carbon* **89** 404–10
- [48] Zhang Q, Wang X j, Meng P, Yue H x, Zheng R t, Wu X L and Cheng G A 2018 *Appl. Phys. Lett.* **112** 013101
- [49] Garcia E J, Wardle B L and John Hart A 2008 *Composites A* **39** 1065–70
- [50] Kalfon-Cohen E *et al* 2018 *Compos. Sci. Technol.* **166** 160–8
- [51] Fan S, chline M G, Franklin N R, Tomblor T W, Cassell A M and Dai H 1999 *Science* **283** 512–4
- [52] De Volder M F L, Vansweevelt R, Wagner P, Reynaerts D, Van Hoof C and Hart A J 2011 *ACS Nano* **5** 6593–600
- [53] Yemini R, Muallem M, Sharabani T, Teblum E, Gofer Y and Nessim G D 2016 *J. Phys. Chem. C* **120** 12242–8
- [54] Yemini R, Itzhak A, Gofer Y, Sharabani T, Drela M and Nessim G D 2017 *J. Phys. Chem. C* **121** 11765–72
- [55] Avraham E S, Westover A S, Itzhak A, Shani L, Mor V, Girshevitz O, Pint C L and Nessim G D 2018 *Carbon* **130** 273–80
- [56] Ahn H S, Sinha N, Zhang M, Banerjee D, Fang S and Baughman R H 2006 *J. Heat Transfer* **128** 1335–42
- [57] Bedewy M, Meshot E R, Guo H, Verploegen E A, Lu W and Hart A J 2009 *J. Phys. Chem. C* **113** 20576–82
- [58] Stein I Y and Wardle B L 2016 *Phys. Chem. Chem. Phys.* **18** 694
- [59] Liu L, Ma W and Zhang Z 2011 *Small* **7** 1504–20
- [60] Lim Y D, Grapov D, Hu L, Kong Q, Tay B K, Labunov V, Miao J, Coquet P and Aditya S 2018 *Nanotechnology* **29** 075205
- [61] Stein I Y, Lewis D J and Wardle B L 2015 *Nanoscale* **7** 19426–31
- [62] Stein I Y and Wardle B L 2016 *Nanotechnology* **27** 035701
- [63] Natarajan B, Lachman N, Lam T, Jacobs D, Long C, Zhao M, Wardle B L, Sharma R and Liddle J A 2015 *ACS Nano* **9** 6050–8
- [64] Huang T, Jiang K, Li L, Chen S, Li R, Shen G and Chen D 2018 *ChemElectroChem* **5** 1652–7
- [65] Yang M, Kim D H, Klein T R, Li Z, Reese M O, Tremolet de Villers B J, Berry J J, van Hest M F A M and Zhu K 2018 *ACS Energy Lett.* **3** 322–8
- [66] Shin D and Tawfick S 2018 *Langmuir* **34** 6231–6
- [67] Tawfick S, Hart A J and De Volder M 2012 *Nanoscale* **4** 3852–6
- [68] Grinthal A, Kang S, Epstein A, Aizenberg M, Khan M and Aizenberg J 2012 *Nano Today* **7** 35–52
- [69] Hart A J and Slocum A H 2006 *J. Phys. Chem. B* **110** 8250–7
- [70] Stein I Y and Wardle B L 2014 *Carbon* **68** 807–13
- [71] Lee J, Stein I Y, Kessler S S and Wardle B L 2015 *ACS Appl. Mater. Interfaces* **7** 8900–5
- [72] Stein I Y, Kaiser A L, Constable A J, Acauan L and Wardle B L 2017 *J. Mater. Sci.* **52** 13799–811
- [73] Lee J, Stein I Y, Devoe M E, Lewis D J, Lachman N, Kessler S S, Buschhorn S T and Wardle B L 2015 *Appl. Phys. Lett.* **106** 053110
- [74] Lachman N, Stein I Y, Ugur A, Lidston D L, Gleason K K and Wardle B L 2017 *Nanotechnology* **28** 24LT01
- [75] Stein I Y, Lachman N, Devoe M E and Wardle B L 2014 *ACS Nano* **8** 4591–9
- [76] Stein I Y and Wardle B L 2013 *Phys. Chem. Chem. Phys.* **15** 4033–40
- [77] Mutha H K, Lu Y, Stein I Y, Cho H J, Suss M E, Laoui T, Thompson C V, Wardle B L and Wang E N 2017 *Nanotechnology* **28** 05LT01
- [78] Jiang D, Wang T, Chen S, Ye L and Liu J 2013 *Microelectron. Eng.* **103** 177–80
- [79] Py C, Bastien R, Bico J, Roman B and Boudaoud A 2007 *Europhys. Lett.* **77** 44005
- [80] Qiu J, Terrones J, Vilatela J J, Vickers M E, Elliott J A and Windle A H 2013 *ACS Nano* **7** 8412–22
- [81] Lim X, Foo H W G, Chia G H and Sow C H 2010 *ACS Nano* **4** 1067–75
- [82] Liu L, Yuan Y, Deng W and Li S 2018 *J. Chem. Phys.* **149** 104503
- [83] Salvetat J P, Bonard J M, Thomson N, Kulik A, Forro L, Benoit W and Zuppiroli L 1999 *Appl. Phys. A* **69** 255–60
- [84] Cebeci H, Stein I Y and Wardle B L 2014 *Appl. Phys. Lett.* **104** 023117
- [85] Lidston D L 2017 Synthesis, characterization, and mode I fracture toughness of aligned carbon nanotube polymer matrix nanocomposites *Master's Thesis* Massachusetts Institute of Technology [hdl.handle.net/1721.1/112473](https://hdl.handle.net/1721.1/112473)

# Supplementary Material: Morphology control of aligned carbon nanotube pins formed via patterned capillary densification

Ashley L. Kaiser,<sup>\*,†</sup> Itai Y. Stein,<sup>‡</sup> Kehang Cui,<sup>¶</sup> and Brian L. Wardle<sup>\*,‡</sup>

<sup>†</sup>*Department of Materials Science and Engineering, Massachusetts Institute of Technology,  
Cambridge, Massachusetts 02139, USA.*

<sup>‡</sup>*Department of Aeronautics and Astronautics, Massachusetts Institute of Technology,  
Cambridge, Massachusetts 02139, USA.*

<sup>¶</sup>*Department of Mechanical Engineering, Massachusetts Institute of Technology,  
Cambridge, Massachusetts 02139, USA.*

E-mail: kaisera@mit.edu; wardle@mit.edu

# S1 Pin Geometry Modeling

The capillary-mediated self-organization of patterned, vertically-aligned carbon nanotube (CNT) arrays into solid pins is modeled based on previous work detailing the one-dimensional (1D) capillary densification of bulk-scale CNT arrays into cellular networks.<sup>1</sup> In this framework, only geometric distinctions related to the pattern size differentiate model development for pin and cellular networks. Since pin formation is defined as occurring within the 1D critical pattern size ( $s_{\text{cr}}$ ) to yield solid CNT structures (see figure S1a), pin formation is subject to a different side-wall boundary condition compared to bulk-scale densification. In this work, pin walls are formed in long, non-isotropic patterns (see figure S1b) as opposed to square or cylindrical patterns, which would involve CNT densification in two dimensions. Therefore, pin formation is modeled *via* the same 1D densification mechanism as bulk-scale cell networks owing to similar underlying physics. As discussed in the main text, the morphological differences between CNT pins and bulk-scale cells is attributed to smaller effective elastic pin wall moduli and densification factors due to the geometric constraint of  $s_{\text{cr}}$ .

With this framework established, the model describing the capillary densification of patterned CNT arrays begins akin to cell formation<sup>1</sup> by considering the maximum fiber bundle size ( $N_{\text{max}}$ ), which was previously derived for the self-assembly of thoroughly-wetted fibers subject to capillary forces:<sup>2-4</sup>

$$N_{\text{max}} = \left(\frac{\gamma}{E}\right)^{2/3} \left(\frac{4h^{8/3}}{D_{\text{cnt}}^2 \Gamma_i^{4/3}}\right) \quad (\text{S1})$$

Here,  $\gamma$  is the surface tension of the solvent,  $E$  is the effective axial elastic modulus of the densified fiber wall (here aligned CNTs),  $h$  is the CNT height,  $D_{\text{cnt}}$  is the CNT outer diameter ( $\sim 8$  nm),<sup>5</sup> and  $\Gamma_i$  is the as-grown inter-CNT spacing ( $\sim 60 - 80$  nm).<sup>5-7</sup> The effective elastic modulus of aligned CNT arrays is a function of the CNT volume fraction ( $V_f$ ), waviness ratio, and interactions due to CNT-CNT junctions,<sup>8,9</sup> which leads to non-negligible CNT-CNT frictional effects during densification.<sup>9</sup> Since inter-fiber adhesion affects the self-organization

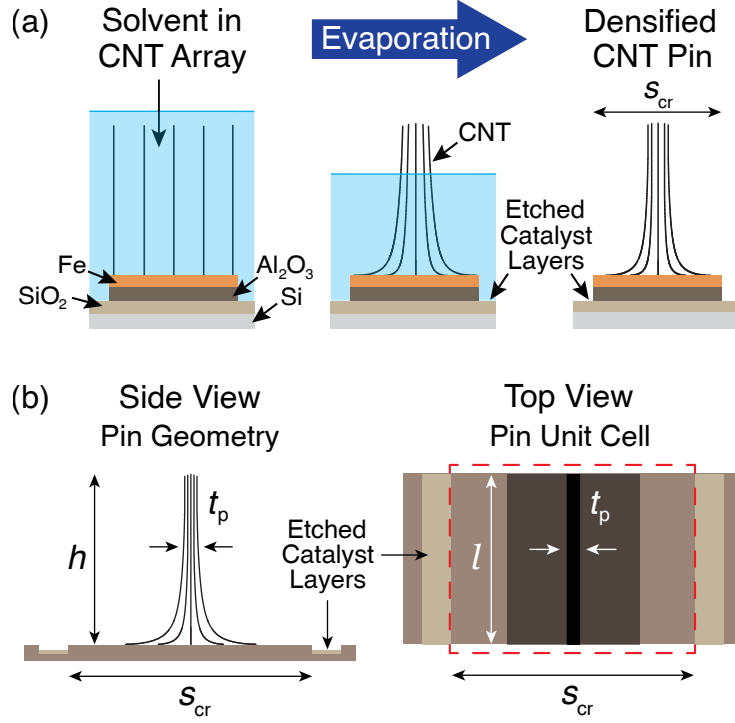


Figure S1: Overview of carbon nanotube (CNT) pin densification and modeling geometry. (a) One-dimensional (1D) illustration showing an aligned CNT array on a patterned substrate undergoing CNT self-assembly as the solvent evaporates, shown here for CNTs with the tangled upper carbon crust removed *via* O<sub>2</sub> plasma treatment. (b) Side view illustration showing the CNT pin height ( $h$ ), critical pattern size ( $s_{cr}$ ), and pin wall thickness ( $t_p$ ), and top view illustration showing  $t_p$  resulting from 1D densification and the pin unit cell of size  $s_{cr} \times l$  used in equation S3, where  $l \gg s_{cr}$  to consider only 1D effects.

of nanofibers into cellular networks and bundles,<sup>10–13</sup> the bending stiffness scaling for CNT pin walls (as in cell walls)<sup>1</sup> is expected to scale as  $N^3$  for this 1D geometry, while scaling as  $N$  is expected when frictional effects are ignored.<sup>4</sup> Therefore, equation S1 corresponds to  $N_{max}^3$ , and the CNT pin wall thickness ( $t_p$ ) can be estimated as follows:<sup>1</sup>

$$t_p = N_{max} \Gamma_f \quad (S2a)$$

$$\hookrightarrow t_p = \Gamma_f \left( \left( \frac{\gamma}{E_p} \right)^{2/3} \left( \frac{4h^{8/3}}{D_{cnt}^2 \Gamma_i^{4/3}} \right) \right)^{1/3} \quad (S2b)$$

where  $\Gamma_f$  is the final inter-CNT spacing within the CNT pin wall, reflecting the degree of CNT densification, and  $E_p$  is the effective axial elastic modulus of the pin wall. Assuming

that all of the CNTs in the original pattern of size  $s_{\text{cr}}$  densify into the final pin structure, the densification factor ( $\Xi_{\text{p}}$ ) and  $s_{\text{cr}}$  can be defined as follows:

$$\Xi_{\text{p}} = \frac{s_{\text{cr}}}{t_{\text{p}}} \quad (\text{S3a})$$

$$s_{\text{cr}} = t_{\text{p}}\Xi_{\text{p}} \quad (\text{S3b})$$

Here,  $\Xi_{\text{p}}$  describes the increase of CNT array packing density as a result of elasto-capillary self-organization and is equal to the final CNT volume fraction within the pin wall. Finally, to enable the full use of equation S2,  $\Gamma_{\text{f}}$  can be approximated as shown below by incorporating  $\Xi_{\text{p}}$  and the as-grown CNT volume fraction ( $V_{\text{f}} \sim 1\%$ )<sup>5,6</sup> into the previously-derived functional form of the inter-CNT spacing scaling as a function of the CNT waviness:<sup>6-8</sup>

$$\Gamma_{\text{f}} = \Omega D_{\text{cnt}} \left( (11.77(3.2(\Xi V_{\text{f}})^{0.6} + 4.1)^{-3.042} + 0.9496) \sqrt{\frac{\sqrt{3}\pi}{6\Xi V_{\text{f}}} - 1} \right) \quad (\text{S4a})$$

$$\Omega = -0.002\Xi V_{\text{f}} + 1.072 \quad (\text{S4b})$$

where  $\Omega$  is the waviness correction factor developed from a three-dimensional stochastic simulation of the packing morphology of wavy CNTs.<sup>7</sup> Equations S2b and S3b are reproduced in the main text for comparison with experimental values.

## S2 Effective Elastic Modulus and Densification Factor Scaling for Non-O<sub>2</sub>-Plasma-Treated CNT Pins

Figure S2 shows the scaling of  $E_{\text{nO}}$  (estimated from equation S2b) and  $\Xi_{\text{nO}}$  (estimated from equation S3a) with  $h$  for CNT pins that were not treated O<sub>2</sub> plasma prior to densification (*i.e.* nO-CNTs).  $E_{\text{nO}}$  scaling can be estimated as  $E_{\text{nO}} \propto \alpha(h)^\psi$  with  $\alpha \approx 3.0 \pm 2 \times 10^{-3}$  and  $\psi \approx 8/3$ , and  $\Xi_{\text{nO}}$  scaling can be estimated as  $\Xi_{\text{nO}} \propto \beta(h)^\omega$  with  $\beta \approx 3.0 \pm 2$  and  $\omega \approx 0.5$ . Here, nO-CNTs experience an additional constraint compared to O<sub>2</sub>-treated CNTs (O-CNTs) during pin formation due to the presence of the upper carbon crust arising from the growth process, which causes greater variability in  $E_{\text{nO}}$  and  $\Xi_{\text{nO}}$ . This constraint limits the overall CNT mobility and packing efficacy, yielding larger  $t_p$  and smaller  $E_{\text{nO}}$ , as discussed in the main text. This effect can be reduced at larger  $h$  due to the enhanced ability of longer CNTs to densify *via* elasto-capillary pairing due to increases in CNT surface area.<sup>2,14</sup>

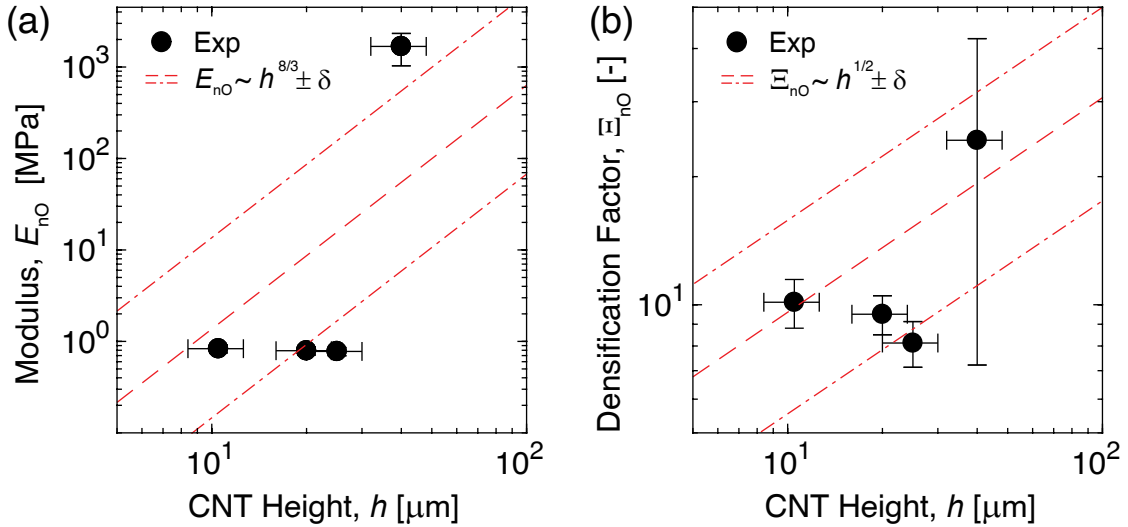


Figure S2: Parameters describing pin formation from non-O<sub>2</sub>-plasma-treated CNTs (nO-CNTs). Plots show the evolution with CNT height ( $h$ ) of (a) the effective pin wall axial elastic modulus ( $E_{\text{nO}}$ ) and (b) the densification factor ( $\Xi_{\text{nO}}$ ). Higher variability is attributed to the carbon crust, which causes structural inhomogeneities within the CNT array.

# S3 Pin Geometry as a Function of Carbon Nanotube Array Height

Table S1 presents the raw data that were evaluated experimentally (*i.e.* ‘Measured’), and the values that result from equations S1 - S4 in section S1 (*i.e.* ‘Calculated’). These data are also presented in figure S2 and figures 2 and 3 in the main text.

Table S1: Experimentally-determined carbon nanotube (CNT) pin height ( $h$ ), pin wall thickness ( $t_p$ ), and critical pattern size ( $s_{cr}$ ) in addition to the calculated pin wall effective axial elastic modulus ( $E_p$ , estimated from equation S2b), and densification factor ( $\Xi_p$ , estimated from equation S3a) for non-O<sub>2</sub>-plasma-treated CNTs (nO-CNTs, ‘No O<sub>2</sub>’) and O<sub>2</sub>-plasma-treated CNTs (O-CNTs, ‘O<sub>2</sub>’), along with standard error. These data originate from CNT array densification with acetone-soaked paper, as discussed further in the main text.

	Measured			Calculated	
	$h$ [ $\mu\text{m}$ ]	$t_p$ [ $\mu\text{m}$ ]	$s_{cr}$ [ $\mu\text{m}$ ]	$E_p$ [MPa]	$\Xi_p$ [-]
No O <sub>2</sub>	11 ± 2	6.1 ± 2	62 ± 30	0.83 ± 0.08	10.1 ± 1.2
	20 ± 4	11 ± 3	105 ± 10	0.79 ± 0.08	9.55 ± 1.0
	25 ± 5	14 ± 3	110 ± 10	0.78 ± 0.08	7.86 ± 1.0
	40 ± 8	11 ± 8	140 ± 20	1700 ± 700	24.4 ± 17
O <sub>2</sub>	13 ± 2	5.8 ± 0.1	50 ± 5	2.6 ± 0.6	8.6 ± 0.6
	20 ± 4	7.3 ± 0.7	90 ± 10	4.9 ± 0.5	12.3 ± 1.3
	25 ± 5	6.4 ± 0.6	110 ± 10	22 ± 2	16.4 ± 1.6
	43 ± 7	7.2 ± 2	150 ± 50	130 ± 30	22.0 ± 2.3

## References

- (1) Kaiser, A. L.; Stein, I. Y.; Cui, K.; Wardle, B. L. Process-morphology scaling relations quantify self-organization in capillary densified nanofiber arrays. *Phys. Chem. Chem. Phys.* **2018**, *20*, 3876–3881.
- (2) Tawfick, S. H.; Bico, J.; Barcelo, S. Three-dimensional lithography by elasto-capillary engineering of filamentary materials. *MRS Bull.* **2016**, *41*, 108–114.
- (3) Chiodi, F.; Roman, B.; Bico, J. Piercing an interface with a brush: Collaborative stiffening. *Europhys. Lett.* **2010**, *90*, 44006.
- (4) Py, C.; Bastien, R.; Bico, J.; Roman, B.; Boudaoud, A. 3D aggregation of wet fibers. *Europhys. Lett.* **2007**, *77*, 44005.
- (5) Lee, J.; Stein, I. Y.; Devoe, M. E.; Lewis, D. J.; Lachman, N.; Kessler, S. S.; Buschhorn, S. T.; Wardle, B. L. Impact of carbon nanotube length on electron transport in aligned carbon nanotube networks. *Appl. Phys. Lett.* **2015**, *106*, 053110.
- (6) Stein, I. Y.; Wardle, B. L. Coordination Number Model to Quantify Packing Morphology of Aligned Nanowire Arrays. *Phys. Chem. Chem. Phys.* **2013**, *15*, 4033–4040.
- (7) Stein, I. Y.; Wardle, B. L. Packing morphology of wavy nanofiber arrays. *Phys. Chem. Chem. Phys.* **2016**, *18*, 694.
- (8) Stein, I. Y.; Lewis, D. J.; Wardle, B. L. Aligned Carbon Nanotube Array Stiffness from Stochastic Three-dimensional Morphology. *Nanoscale* **2015**, *7*, 19426–19431.
- (9) Cebeci, H.; Stein, I. Y.; Wardle, B. L. Effect of Nanofiber Proximity on the Mechanical Behavior of High Volume Fraction Aligned Carbon Nanotube Arrays. *Appl. Phys. Lett.* **2014**, *104*, 023117.
- (10) Picu, R. C.; Sengab, A. Structural evolution and stability of non-crosslinked fiber networks with inter-fiber adhesion. *Soft Matter* **2018**, *14*, 2254–2266.

- (11) Zhou, M.; Chen, K.; Li, X.; Liu, L.; Mo, Y.; Jin, L.; Li, L.; Tian, Y. Clumping Stability of Vertical Nanofibers on Surfaces. *Langmuir* **2018**, *Article ASAP*.
- (12) Pokroy, B.; Kang, S. H.; Mahadevan, L.; Aizenberg, J. Self-Organization of a Mesoscale Bristle into Ordered, Hierarchical Helical Assemblies. *Science* **2009**, *323*, 237–240.
- (13) Shin, D.; Tawfick, S. Polymorphic Elastocapillarity: Kinetically Reconfigurable Self-Assembly of Hair Bundles by Varying the Drain Rate. *Langmuir* **2018**, *34*, 6231–6236.
- (14) De Volder, M.; Park, S. J.; Tawfick, S. H.; Vidaud, D. O.; Hart, A. J. Fabrication and electrical integration of robust carbon nanotube micropillars by self-directed elastocapillary densification. *J. Micromech. Microeng.* **2011**, *21*, 045033.